Optics & Laser Technology 179 (2024) 111362

Contents lists available at ScienceDirect

Optics and Laser Technology

journal homepage: www.elsevier.com/locate/optlastec

Full length article

Nonthermal ablation of crystalline c-cut Sapphire using femtosecond deep UV laser pulses

Dominyka Stonyte *, Vytautas Jukna, Darius Gailevicius, Domas Paipulas

Laser Research Center, Faculty of Physics, Vilnius University, Sauletekio av. 10, LT 10223, Vilnius, Lithuania

ARTICLE INFO

Keywords:
Laser ablation
High harmonics
Deep UV
Femtosecond
Sapphire
Fifth harmonic
High bandgap
Non-thermal ablation

ABSTRACT

The demand for precise and high-quality machining of wide-bandgap materials, such as glasses and crystals, is of considerable significance in science and industry. Among these materials, sapphire stands out as an appealing choice due to its exceptional mechanical and optical attributes, high thermal conductivity and stability, low electrical conductivity, and resilience against harsh chemicals. Despite its hardness, sapphire is brittle, making it prone to cracking during conventional machining attempts. Recently, alternative non-contact approaches, like laser ablation, have emerged as potential solutions to improve the machining quality. However research of laser processing of wide-bandgap materials, especially utilizing the high harmonics of femtosecond solid-state laser systems, remains incomplete. Our study focuses on investigating the nonthermal laser ablation of c-cut sapphire crystals using femtosecond (300 fs) deep UV (206 nm) laser pulses and comparing the results with traditional IR femtosecond ablation. The publication encompasses a comprehensive depiction of the ablation process and a review of the various achieved morphologies with accompanying scanning electron microscope images. Our findings indicate that efficient ablation with surface roughness below 100 nm can be achieved through a single-step process within specific laser processing parameter ranges. The ablation process of sapphire encompasses a strong incubation effect, hence the pulses need to be tightly overlapped. Additionally, we provide a detailed description of methodology used to extract surface roughness which was utilized in all the presented research and offers a practical framework for characterizing ablation results obtained from diverse laser systems.

1. Introduction

Sapphire is one of the most resilient and toughest materials known, meaning it is highly scratch-resistant and durable. In addition, it exhibits excellent optical properties [1–3] having a broad transmission spectrum including near UV, VIS, and near IR. This allows the transmission of light with minimal absorption, which makes it ideal for optical applications. Sapphire also has high thermal stability and excellent thermal conductivity, it can also withstand high temperatures (melting point 2050 °C) [4] and rapid temperature changes without damage, making it appropriate for high-temperature environments. Its low electrical conductivity makes it suitable for applications where good electrical insulation is needed. Sapphire can also be exposed to harsh chemical environments as it is resistant to most acids. All of these advantages make this material one of the most desirable to apply in almost every field: military (bulletproof glass [5]), space industry (satellite windows, optical systems, gyroscopes [6]), electronics (light-emitting diodes, radio frequency devices [7]), everyday-use devices (watch crystals, displays of mobile devices, protection windows for cameras [8]), optics (optical lenses, windows, micro-optics, diffractive optical elements [9]). The primary methods of sapphire processing are mechanical in nature and involve diamond grinding [10], diamond cutting [11,12], and chemical mechanical polishing [13], among others. However, these techniques suffer from certain drawbacks, such as tool wear and limitations imposed by the geometry of blades used; in most cases, cooling is required; it can also be challenging to make small sub-micrometer or sub-nanometer features. In contrast, non-contact processes such as laser processing could be advantageous compared to mechanical methods [2].

Laser processing of sapphire can be challenging due to low linear absorption of the material i.e. wide bandgap. One approach is to use intense ultrashort ps/fs laser pulses and deposit laser energy via non-linear absorption process, which leads to removal of the material if enough energy is absorbed [14]. In addition, laser ablation using femtosecond pulses is, in most cases, a non-thermal process, as a pulse-lattice interaction time is much shorter than heat transfer to the lattice, so the pulse ends even before thermal and structural effects occur [15]. Nevertheless to achieve efficient and low roughness laser ablation of high-bandgap materials and simultaneously ablate deeply into the material (several micrometers per pass and more) is a challenge. Mostly all

* Corresponding author.
E-mail address: dominyka.stonyte@ff.vu.lt (D. Stonyte).

https://doi.org/10.1016/j.optlastec.2024.111362
Received 20 February 2024; Received in revised form 22 May 2024; Accepted 20 June 2024
Available online 2 July 2024

of the low roughness ablation techniques use additional technological step which acts as a polishing step. For example Yang et al. [16] proposed a novel dual-beam laser induced plasma assisted ablation (LIPAA) technique to control nanoparticle generation, resulting in enhanced sapphire femtosecond laser processing. They have successfully demonstrated that this method can reduce the ablation threshold of resulting structures. Obtained roughness values were in the 18.1 – 30 nm range while achievable ablation depth was only in submicron range. However, there is a large demand from many technological applications for deeper and quicker processing of sapphire.

An appealing approach to processing materials with high bandgaps, such as sapphire, is ablation using ultraviolet (UV) laser pulses. As the photon energy is inversely proportional to laser wavelength the UV photon energy can greatly reduce the multi photon absorption order or even induce linear absorption in high bandgap materials. This technique was tested with the use of longer nanosecond/picosecond pulses of excimer or q-switched solid-state UV lasers [17–20]. Crunteanu et al. [21] structured sapphire by direct laser ablation using nanosecond ArF excimer (193 nm) laser and made 2.5 μm deep, relatively smooth channels. However, the channel sidewalls had a rough surface due to extensive melting and re-solidification which occurred at the boundaries of ablated areas. Wei et al. [22] polished a sapphire sample using a Q-switched 355 nm UV picosecond laser and achieved roughness Ra values of 104 nm. Hideyuki et al. [23] utilized the fifth harmonic of Nd:YAG laser (213 nm) generating 5 ns duration pulses with 10 Hz repetition rate and showed significant reduction of thermal damage compared to ablation with longer wavelength pulses. They have achieved roughness values ranging from 200 nm to 1 μm depending on the laser pulse energy used. Wang et al. [24] studied a material removal mechanisms of c-plane sapphire during nanosecond UV laser ablation and showed that material removal is caused mainly by thermal effects, including sublimation, vaporization, melt, and sputtering by the accompanied plasma. As was mentioned before, ablation using femtosecond pulses is a non-thermal process so it could result in the dramatic reduction of heat affected zones (HAZ) and unwanted resolidified melt flow. However, laser processing using UV ultrashort femtosecond laser pulses has seldom been studied. We have also observed, that most of the research done with UV pulses where surface roughness was measured was done on the pre-polished or planar samples. The removed material thickness ranged only from tens or hundreds of nanometers. Therefore the utilization of UV pulses was shown only for post-polishing process and was relatively slow. Deep micro structuring is greatly needed in the technological applications. In that case, it is achieved in two steps: the first is laser ablation, and the second is polishing. The later can be performed not only by laser micro machining, but also may include chemical etching [25], high-temperature annealing [26].

To our knowledge, no research exists in laser processing of sapphire using deep UV femtosecond pulses. In this paper, we show that the use of 5th harmonic (206 nm) of a femtosecond (300 fs) Yb:KGW laser system with a pulse repetition rate of 50 kHz results in significantly better results when ablating c-cut sapphire if compared to longer pulses and longer wavelengths. We demonstrate a high throughput of one-step process, a several micrometers deep microstructures having a low roughness (87 nm and higher) achieved by one scanning pass. This would alleviate the need of additional polishing step. To show the many advantages of the UV pulses we have compared the same microstructuring with comparable focusing conditions but longer wavelength (1030 nm). Our results indicate that laser ablation with ultrashort deep UV pulses can be used for making diffractive optical elements, microfluidics, functional micro-optics, etc.

2. Experimental

2.1. Experimental setup

Deep UV ablation experiments were conducted by generating 5th harmonic of an ultrashort pulsed solid-state Yb:KGW laser (Pharos, Light Conversion LTD) radiation. Laser was working at the repetition rate of 50 kHz generating 300 fs laser pulses at 1030 nm. The commercially available 5th harmonic module was directly mounted on the laser to convert fundamental wavelength to 5th harmonic (206 nm). The experimental setup is shown in Fig. 1(a). Laser beam is directed by dielectric mirrors to the focusing optics, in this case, CaF_2 lens with a focal length of 25 mm. The focusing lens is mounted on a vertical micro-positioning stage Aerotech ANT180. The beam is focused on the sample placed on a micro-positioning system consisting of two micro-positioning stages Aerotech ANT180, stacked on top of each other to produce a transversal movement in the xy plane. DMC (Direct Machining Control, Ltd.) software was used to automate fabrication. As the stages tend to vibrate if accelerated too quickly, this vibration can induce unwanted geometry errors. To reduce this wobble effect, stages were accelerated for a 2 mm distance before firing laser pulses using the velocity stabilization function provided in the DMC software package. Due to a lack of commercially available deep UV attenuators, a custom approach to beam attenuation was used. We have manually placed UV grade fused silica glass plates of 0.3 mm thickness to the beam path. The beam was attenuated due to accumulation of losses due to surface reflections.

We have also used fundamental frequency of the Yb:KGW laser for micro machining experiments to be able to compare the results. The slightly shorter pulse duration (240 fs) and higher repetition rate of 100 kHz (Pharos, Light Conversion) laser was used (see Fig. 1(b)). The beam is attenuated using a common attenuator which consists of a half-wave plate, polarizing beam splitter cube and beam dump. We have made the beam width of the fundamental beam on the sample to be equal to 5th harmonic beam by constructing a telescope and choosing an appropriate focusing lens. The positioning of the sample was made with the same Aerotech ANT 180 positioning stages. Therefore we could use identical micro machining algorithms for both setups.

The fifth harmonic's beam diameter (at $1/e^2$ intensity level) in front of the lens was $2\omega_0 = 0.594$ mm, where ω_0 is the beam radius, and it was measured using a CCD camera Spiricon SP503U, Ophir, (the result is depicted in the inset of Fig. 2(a)). The beam diameter on the sample (focused) was measured using Liu method [27] and for this purpose, several pits were ablated on BK7 glass sample surface with varying pulse energies. The squared pit diameter dependence on laser pulse energy in logarithmic axis is depicted in Fig. 2(a). The slope of a linear fit is equal to $2\omega_0^2$ and consequently the beam diameter was found to be $2\omega_0 = 6.58$ μm. The beam diameter at the focus is slightly larger than calculated from Gaussian optics, but this can come from the reduced quality of the beam when fundamental wave is converted to 5th harmonic, and also due to optical aberration induced by focusing system.

The first harmonic's beam diameter in front of the lens is $2\omega_0 = 1.559$ mm and it was measured using Spiricon SP932U beam profiler (see the inset of Fig. 2(b)). The focused beam diameter was measured using the same Liu technique [27], but pits were ablated on the Ag coated soda-lime glass. The retrieved beam diameter was 6.62 μm and is very close to the focused 5th harmonic beam diameter.

The average power in both cases was measured using a Nova II, Ophir power meter. To clean all the samples from the ablation debris they were immersed in acetone and distilled water solution and placed in an ultrasonic bath for 10–20 min. Topographies were measured using an optical profilometer LEXT OLS 5100 with a 100x magnifying objective with a numerical aperture NA = 0.95 and a working distance WD = 0.35 mm. Samples were also imaged using a scanning electron microscope (SEM) Prisma E, Thermo Fisher.

Experiments were conducted on the surface of a crystalline c-cut Sapphire sample. Parallel grooves of 2 mm in length were ablated with different processing parameters, such as pulse overlap (PO) and energy as depicted in Fig. 3.

The translation speed of the sample relative to the beam was fixed at 5 mm/s, which gave as a 50 nm minimum displacement between

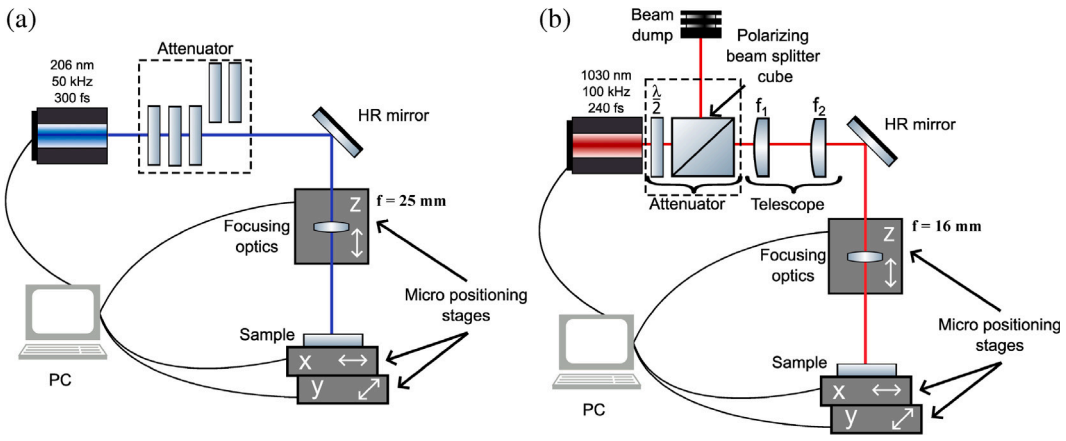

Fig. 1. (a) Deep UV ablation experimental setup, where CaF_2 lens with f = 25 mm is used for focusing; (b) IR ablation experimental setup (f_1 = 150 mm and f_2 = 50 mm), where an objective lens with f = 16 mm is used for focusing.

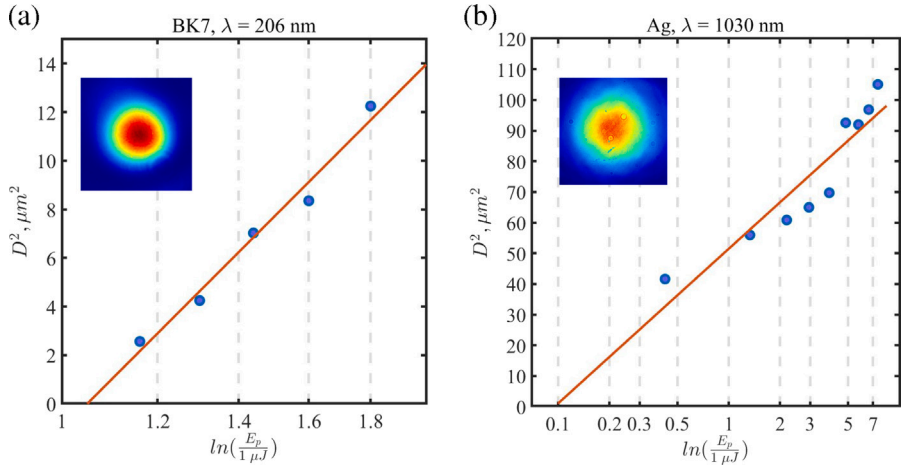

Fig. 2. The dependence of a squared diameter of ablated pits on laser pulse energy [27] in semi-logarithmic scale (x axis), where the insets show a laser beam intensity profile for (a) fifth harmonic, and (b) first harmonic.

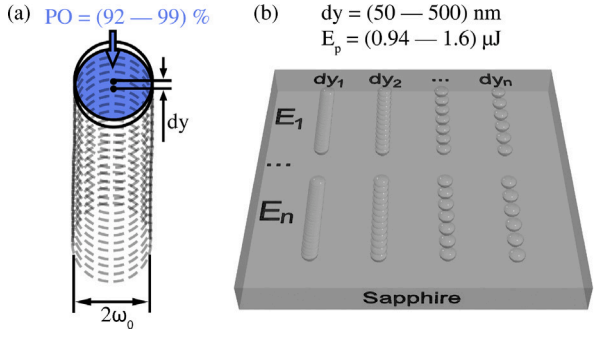

Fig. 3. (a) *dy*, *PO*, and beam diameter parameters, (b) schematic illustration of an experiment.

the pulses at 100 kHz laser repetition rate. The overlap of the pulses was varied by changing the shutter opening intervals, i.e. reducing the laser repetition rate with a pulse divider. PO was calculated using this formula:

$$PO = \left(1 - \frac{dy}{2\omega_0}\right) \times 100\%, \quad (1)$$

where dy is the displacement between pulses, and $2\omega_0$. The influence of pulse energy and PO on grooves' quality, diameter, depth, volume, bottom roughness, ablation efficiency, and edge steepness were estimated by examining their topography data. Data analysis was automated using the Matlab software package.

2.2. Automation of data processing and result evaluation

Each of the ablated grooves topography was measured with an optical profilometer. To assess the fabricated groves parameters each individual topography data underwent procedures which can be grouped into three parts. First part is the removal of measurement setup errors. Second part is the decomposition of morphology to form, and roughness. Third part is the extraction of the fabricated grooves parameters such as depth, width, roughness, and steepness of the groove. The flow chart of the data processing is depicted in Fig. 4(a).

The first part of data processing consisted of these steps. First is the plane removal which comes due to not positioning the sample strictly perpendicular to the measurement setup. Which is consistent with the L-filter in ISO 25178-3:2012 [28] standard and act as a large-scale lateral component removal procedure. Measurement noise is removed according to the same standard, where Gaussian S-filter is used with a nesting index N_{is} value that is 3 times higher than sampling distance. In the measurement data we have observed measurement outliers, that comes due to imperfections of the measurement and are outside the interval of the percentiles 5:95. We removed the identified points by first locating them and then smoothing their values through linear interpolation with neighboring points. The last step in first part of data processing is the rotation of the groove so as all the grooves are parallel

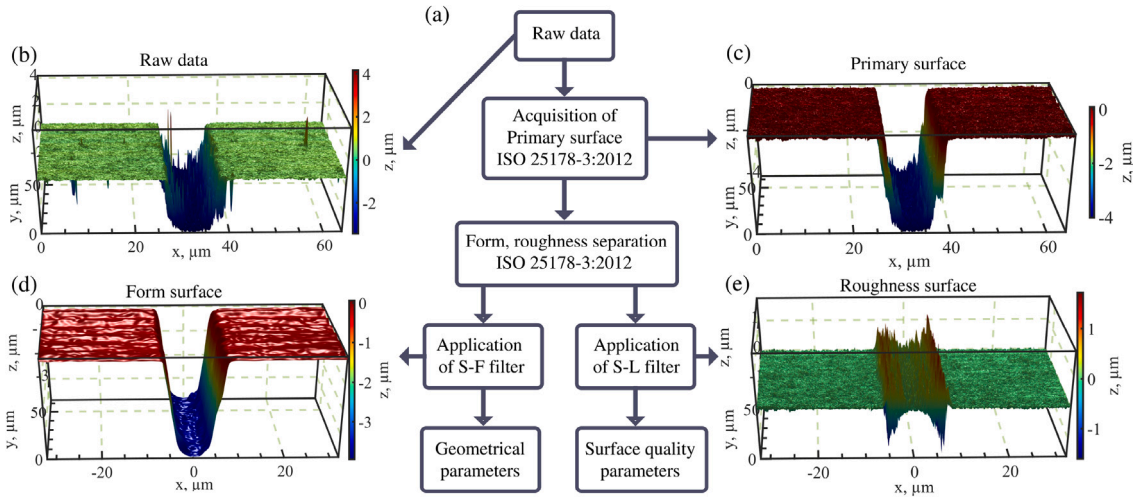

Fig. 4. Data processing steps (PO = 98.48%, E_p = 1.6 µJ): (a) data processing flow chart, (b) the original unprocessed channel's topography data, (c) obtained primary surface from which (d) form, and (e) roughness surfaces are calculated by spatial wavelength filtering according to ISO 25178-3:2012 [28] standard.

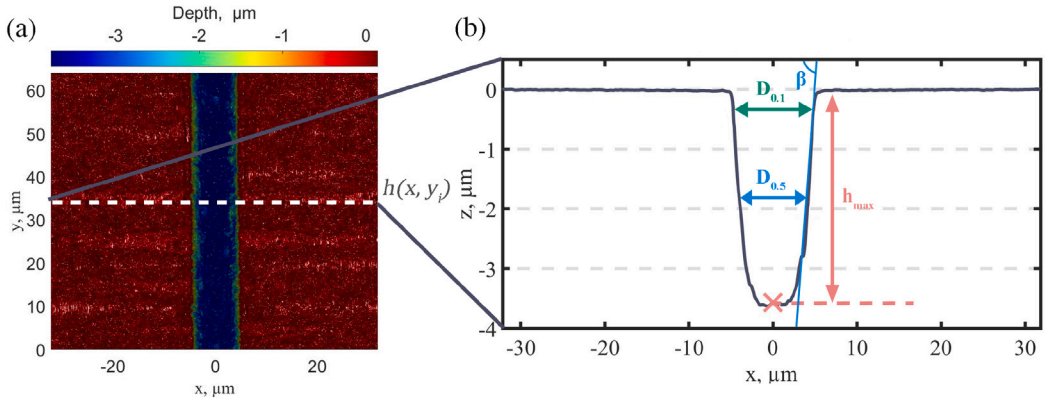

Fig. 5. Geometrical parameter evaluation example (PO = 98.48%, E_p = 1.16 µJ): (a) horizontal profiles are extracted from a form topography data, and (b) parameters are evaluated for each horizontal profile.

to y axis. It was done by calculating the measured groove's ends' mass centers and rotate whole data matrix so as mass centers are positioned at $x = 0$ values. The example of this data manipulation is depicted in Fig. 4(b) and (c).

The form and structure topographies (see Fig. 4(d) and (e)) were separated with the use of additional Gaussian filter with nesting index of N_{if} = 3 µm. Micro channels were characterized with geometrical parameters such as depth, width, volume and steepness. Calculations of these parameters are performed on form topography (see Fig. 4(d)). Whilst surface quality analysis was done by evaluating surface roughness from the structure topography (see Fig. 4(e)).

Grooves' depth, width and side steepness values are average values over the measured length of the grove. We have obtained all the above mentioned parameters for every individual line of topography data and registered average value over the full length of the measured grove. The example of an extracted profile and parameter calculation is depicted in Fig. 5(b). For each of the profile we find three parameters. First is the depth of the groove (h_{max}) which is the value taken at the center (x = 0) of the groove and is depicted by red cross in Fig. 5(b). Second parameter is the width of the groove which is measured at the depth of half of maximum depth ($D_{0.5}$) and is depicted by the blue line. Lastly the groves steepness is measured by finding the angle between the width of the groove at the 10% ($D_{0.1}$) of the maximum depth value, and the depth at half maximum depth ($D_{0.5}$). Then the steepness is calculated as:

$$\beta = \arctan\left(\frac{4h_{max}}{5(D_{0.1} - D_{0.5})}\right) \tag{2}$$

Volume V of ablated material was obtained by integrating the depth:

$$V = \int_{x_{min}}^{x_{max}} \int_{y_{min}}^{y_{max}} |h(x,y)| dx dy, \tag{3}$$

where $h(x, y)$ is a height profile, x_{min} and x_{max} are minimal and maximal x coordinates respectively, y_{min} and y_{max} are minimal and maximal y coordinates respectively. Ablation efficiency is defined as:

$$\eta = \frac{E_{sum}}{V}, \tag{4}$$

where E_{sum} is the energy used to ablate the groove and is equal to

$$E_{sum} = \frac{E_{pulse}(y_{max} - y_{min})}{dy}, \tag{5}$$

where dy is a displacement between pulses.

To assess the manufactured groove quality we have examined the roughness of the groove's surface. Roughness parameters are calculated from roughness surface as is shown in Fig. 6(a).

Groove bottom surface profile is extracted along the $x = 0$ line and is depicted in Fig. 6(a) with a dashed line. From the extracted profile (shown in Fig. 6(b)) the groove bottom roughness Ra is calculated as:

$$Ra(x) = \frac{1}{L} \int_0^L |h(x,y)| dy, \tag{6}$$

where L is the length of a groove, $h(x, y)$ is a height profile [29]. It was observed, that the groove roughness has slight dependence on the position inside the groove. The Ra dependence on coordinate x is

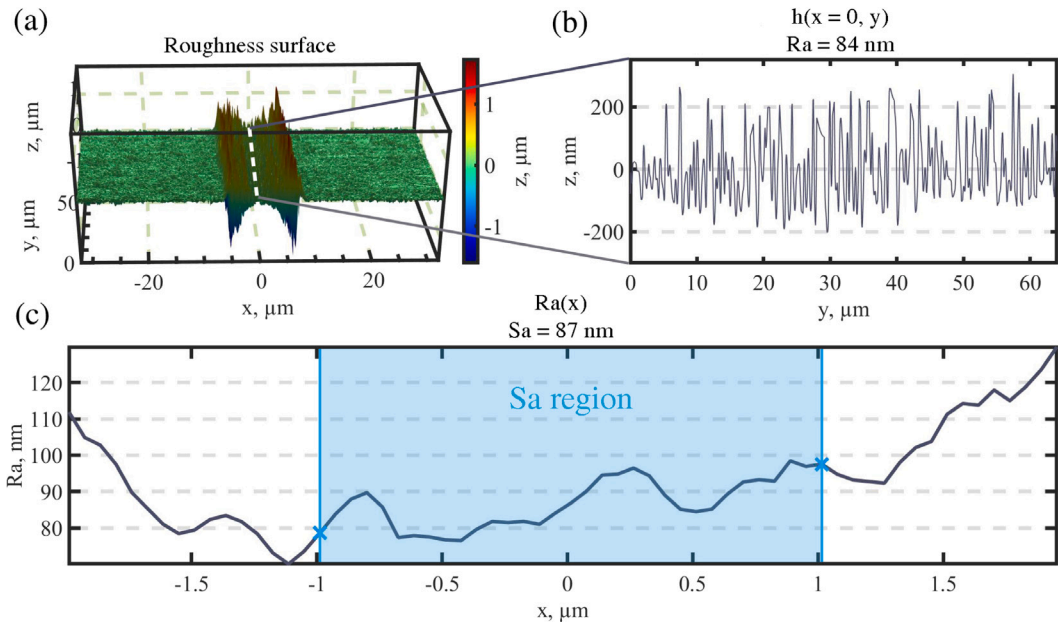

Fig. 6. Roughness calculation (PO = 98.48%, E_p = 1.6 µJ): (a) roughness surface, (b) groove's bottom profile at x = 0, (c) roughness dependence on a profile extraction position.

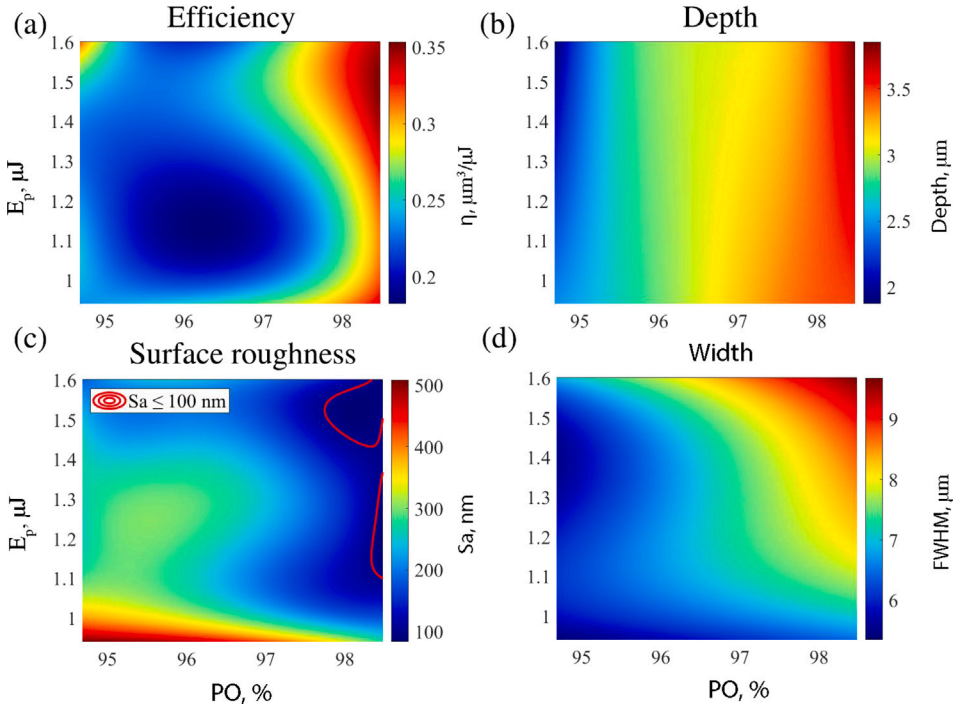

Fig. 7. Parameter maps, depicting the ablated channels (a) efficiency, (b) depth, (c) surface roughness *Sa*, and (d) full width at half maximum dependencies on laser pulse energy E_p and PO.

depicted in Fig. 6(c). The edges of the groove has high variation of the depth, and it partly comes from the measurement and data preparation inaccuracies. Therefore we have chosen to examine the surface quality of the grove bottom by taking 2 µm width bottom region for surface roughness investigation (indicated with a light blue area in Fig. 6(c)). This region is characterized with an arithmetic mean height parameter Sa which is the mean of the absolute of the ordinate values of the scale-limited surface:

$$Sa = \frac{1}{A}\int\int_{\tilde{A}} |h(x,y)| dx dy, \tag{7}$$

where A represents the value of the evaluation area, $\tilde{A}$ represents the domain of integration, and $h(x, y)$ is the height profile [30]. As this areal parameter takes into account a wider range of data, the texture is characterized more accurately. Therefore all the channels are characterized using average surface *area* roughness parameter Sa instead of average surface roughness parameter Ra.

3. Results and discussion

Parameter maps encompassing all the acquired outcomes are presented in Fig. 7. In cases involving micro-structuring, such as fabricating diffractive optical elements and microfluidics, the geometric

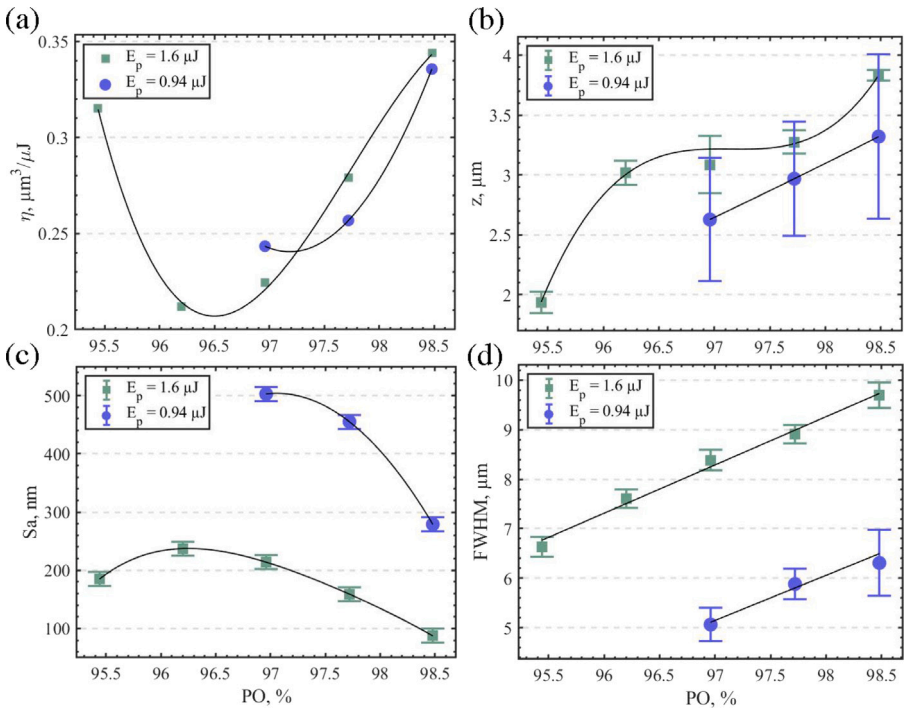

Fig. 8. The ablated channels (a) efficiency, (b) depth, (c) surface roughness Sa, and (d) full width at half maximum dependencies on laser PO for the highest and the lowest pulse energies E_p used.

parameters of structures hold significant importance. These maps serve to characterize the system, enabling the selection of operational ranges and the anticipation of resulting values prior to conducting experiments. With the automation of the process (measurement and post-processing of results), swift and precise characterization of ablation outcomes for other laser systems is feasible. The relatively modest maximal pulse energy values are attributed to the utilization of the 5th harmonic, requiring the fundamental harmonic laser beam to traverse multiple crystals and optical elements, resulting in power attenuation. Although higher pulse energy values are imperative for ablating glasses and crystals using lower harmonics, the UV range ablation of these materials necessitates significantly lower pulse energies due to linear (or two-photon) absorption effects.

A parameter map (depicted in Fig. 7(a)) illustrates the dependence of efficiency on both the number of pulses and PO, revealing two distinct regions: an *inefficient* regime (PO < 97.6%) and an *efficient* regime (PO > 97.6%). Remarkably, the efficient region aligns precisely with the domain where the deepest channels are ablated (refer to Fig. 7(b)) and corresponds to the region of the lowest surface roughness Sa values, indicated by a red contour in Fig. 7(c) for Sa values below 100 nm. In this efficient regime, precise control over the full-width at half-maximum (FWHM) of channels, ranging from 7 to 10 μm (as depicted in Fig. 7(d)), and their depth within 3.5 to 4 μm (as shown in Fig. 7(b)), can be achieved by tuning the laser pulse energy within the range of 1.1 – 1.6 μJ while maintaining low roughness values. This level of depth and width control without compromising quality (roughness) is particularly crucial for ensuring precision in the fabrication of complex geometric structures.

The dependencies of resulting efficiency, depth, average surface roughness *Sa*, and FWHM on PO are illustrated in Fig. 8 for both the highest and the lowest pulse energies employed.

When the pulse energy is set at a higher level, the ablation efficiency decreases with a decreasing PO in the interval of 98.5–96.5% meaning that the ablated volume decreases more rapidly than the sum energy. This phenomenon can be attributed to the nanograting formation (see Fig. 10(b), (c)) process, which is more probable with an increasing laser pulse density. These modifications can have a higher absorption rate of laser energy and act as a seed for the effective laser ablation. Conversely, the ablation efficiency increases with the decrease of PO values in the interval of 96.5-95.5%. When the pulse energy is at the lowest level, the ablation efficiency values are slightly lower if compared to the ones, obtained with the highest pulse energy. In addition, the rapid decrease of efficiency saturates at the 0.5% higher PO value (PO = 97%) if compared to the highest pulse energy.

When the pulse energy is set at a higher level (as depicted in Fig. 8(b)), depth values exhibit growth with increasing PO. Conversely, for lower pulse energies (as shown in Fig. 8(b)), this growth curve levels off, becoming linear. If the pulse energies were to be pushed even higher, there would be a point at which the depth increase saturates due to an increase in the density of free electrons, leading to enhanced reflectivity and plasma shielding. Discrepancies in depth measurement errors become apparent when comparing the lowest pulse energy to the highest, which can be attributed to observations from SEM photos (refer to Fig. 9). Grooves engraved with lower pulse energy tend to retain more ablation residue particles at the bottom compared to those ablated with higher pulse energy. This phenomenon is due to the more efficient and complete material removal associated with higher energy, resulting in a cleaner and smoother groove bottom with fewer residual particles. Furthermore, when ablating with higher pulse energy, any residual particles are expelled farther away from the channel compared to lower energy settings. Consequently, as the depth calculation involves extracting numerous 2D profiles of a groove and averaging them, profiles containing particles at the bottom exhibit shallower depths than cleaner groove sections. As a consequence, the range of depth deviations widens.

Comparing average roughness *Sa* values, those attained with the highest pulse energy (depicted in Fig. 8(c)) are from two to three times lower compared to those obtained with the lowest energy setting. It can clearly be seen, that groove's bottom quality increases with an increasing PO value. However, for PO values higher than the ones, depicted in Fig. 8(c) the quality of a groove dramatically reduces as the sum energy density reaches critical value and the ablated zones, as well as the surrounding material become excessively damaged.

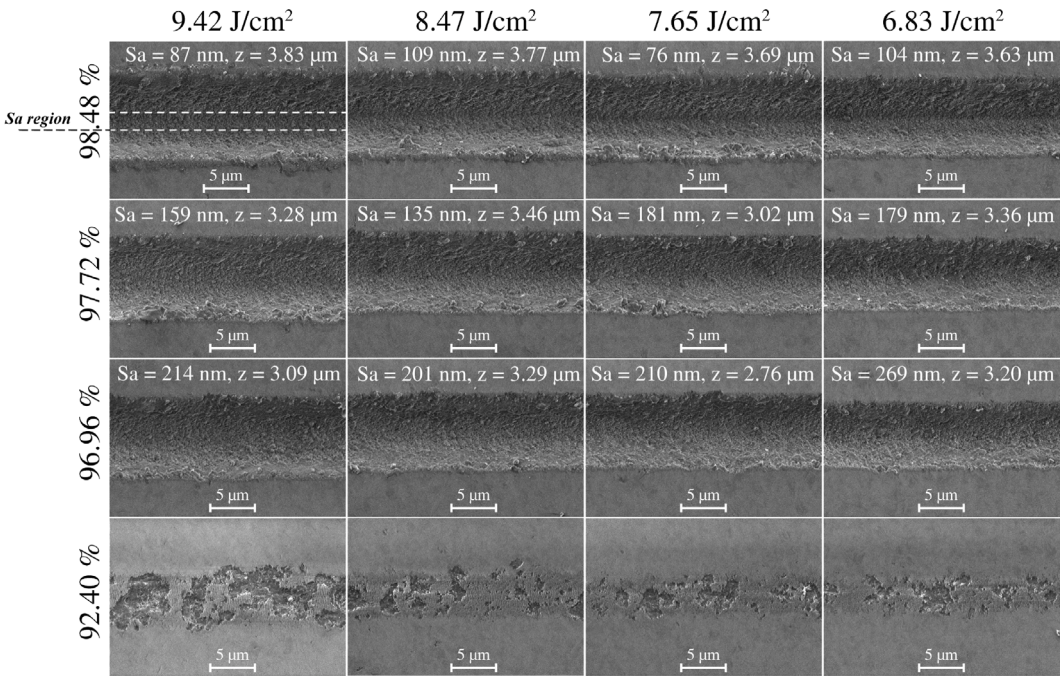

Fig. 9. SEM images of grooves, ablated on the surface of c-cut sapphire, with femtosecond deep UV (257 nm) laser pulses, using different pulse energies (different fluence values) and spacing between pulses (PO values). *Sa* indicates average surface area roughness values and *z* indicates depth values.

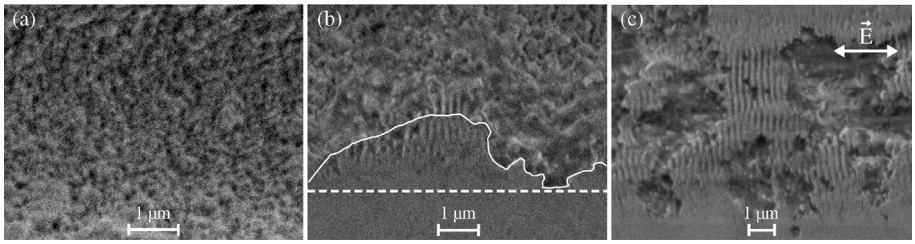

Fig. 10. Features, observed with $F_0 = 9.42$ J/cm^2: (a) nanostructures on a groove's bottom, PO = 98.48%, (b) groove sidewall form deviation (white curved line) from the ideal form (dashed white line), PO = 94.68%, (c) nanograting regions, PO = 92.40%.

The full width at half maximum (FWHM) of the ablated grooves grows at the same speed with an increasing PO for both the highest and the lowest pulse energies employed, as depicted in Fig. 8(d). FWHM values, obtained with the highest pulse energy are 1.5 times higher compared to the ones with the lowest pulse energy.

The steepness values of grooves were observed within the range of 58 – 80° and did not exhibit a clear dependence on either PO or pulse energy.

It is widely acknowledged that when a material is subjected to an incident laser pulse, several interactions occur, encompassing energy absorption, scattering, and reflection. The absorbed energy fraction triggers the generation of free electrons through mechanisms like multi-photon and avalanche ionization processes. When the material's surface is flat, the impact of a Gaussian laser pulse results in free electrons being spatially distributed according to a Gaussian pattern—reaching the highest concentration at the center and progressively diminishing radially outward. This is the reason, why the form of a groove resembles the shape, depicted in Fig. 5(b).

Sapphire, characterized by its wide bandgap properties with a 9.3 eV energy difference between the valence and conduction bands, requires the simultaneous absorption of multiple photons for energy absorption to occur. In the context of a Yb:KGW laser system's first harmonic, which boasts a wavelength of 1030 nm equivalent to 1.2 eV, the successful modification of sapphire mandates an 8-photon absorption process. In contrast, the fifth harmonic, operating at a wavelength of 206 nm corresponding to 6.02 eV, necessitates only a 2-photon absorption for effective ablation. The utilization of a two-photon absorption mechanism yields reduced heat-affected zones and, in turn, can yield superior outcomes compared to multi-photon absorption.

Scanning electron microscopy (SEM) images of grooves formed on sapphire's surface, employing different combinations of pulse energies and PO parameters are depicted in Fig. 9. When pulse energy and PO values are high, groove's shape deviates from Gaussian and the bottom of a groove becomes relatively flat, as shown in Fig. 5(b). This occurs because in the center of a laser spot, the free electron density formed is very high, and most of the laser energy will be reflected by electron plasma. With increased incident depth, the difference of laser intensity between the center of a laser spot and the surrounding area will decrease, making a distribution of free electron density more uniform [31]. Heated plasma plume can also considerably affect surface morphology because it can act as a secondary energy source that provides energy to the surface and increase its deformation [32]. However, when the photon energy is sufficiently high and the pulse duration is sufficiently low, a non-thermal ablation can be realized during which direct bond scissions occur, which can even result in structural lattice changes and the temperature of a lattice remains unchanged during laser irradiation. The absence of melting and explosive evaporation result in high surface quality [15]. Due to the absence of deposited ridges and melt, we presume that thermal processes such as melting and resolidification are not involved.

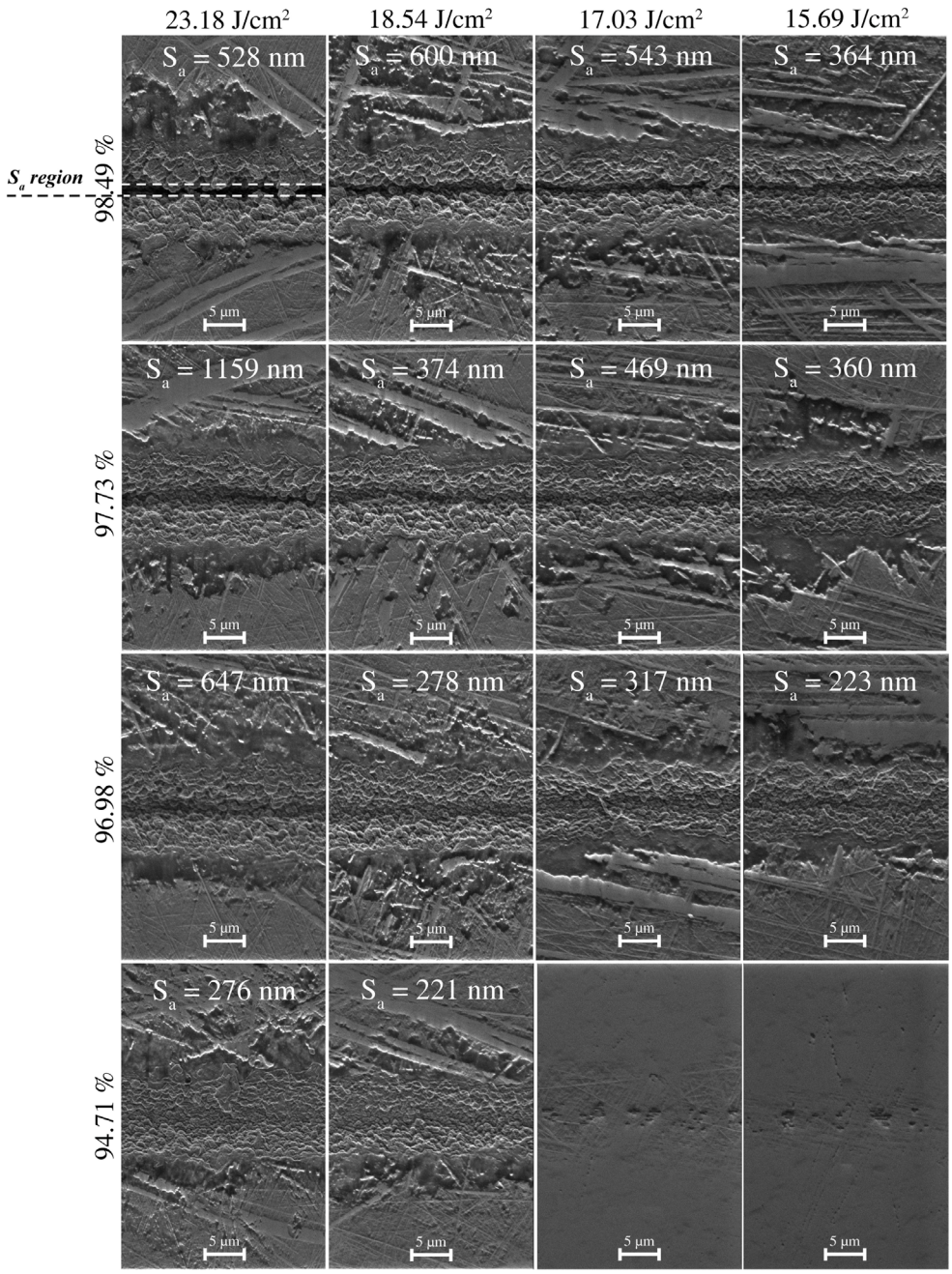

Fig. 11. SEM images of grooves, ablated using $\lambda = 1030$ nm pulses on the surface of c-cut sapphire using different pulse energies (different fluence values) and spacing between pulses (PO values). S_a indicates surface roughness values, measured using a PDMS stamp.

Sapphire samples might not be entirely pure, wherein some randomly distributed impurities and defects, introduced during crystal growth and postgrowth treatment of the surface, can have a higher absorption rate of laser energy than the surrounding material [33]. The modified areas at low energy density (lowest PO of 92.40% in Fig. 9) have a nondeterministic nature of damage suggesting that defects play a significant role in multi-pulse optical damage [34] but establishing that is beyond the scope of this research. With an increasing fluence, modified areas tend to grow and a groove is formed when the energy density is high enough to sustain an effective ablation process.

The main observed features are depicted in Fig. 10. When the PO is relatively high ($PO = 98.48\%$) the morphology of nanostructures, observed in grooves' bottom (see Fig. 10(a)) indicates that the material breakup and ejection mechanism is photomechanical, driven by high amplitude, tensile pressure waves — spallation [35]. With a reduced PO ($PO = 94.68\%$), the sidewalls of a groove start to deviate from the ideal form, which is indicated with a straight line in Fig. 10(b) to a curved form. Nanogratings start to appear near the sidewalls, in low energy density regions and with a further decrease of PO to $PO = 92.40\%$, only small regions of material are ablated and nanogratings are observed in non-ablated regions as is shown in Fig. 10(c). The observed nanogratings are aligned perpendicularly to laser polarization and scanning direction, having a period in the interval of $\Lambda = (155 - 200)$ nm. The ratio of Λ to the laser wavelength λ is in the range of $\Lambda/\lambda = (0.75 - 0.97)$. This ratio corresponds to near-subwavelength ripples (NSRs, $0.4 < \Lambda/\lambda < 1$) [36]. As the laser pulse excites the electrons to the conduction band during the rising edge of the laser pulse, if the lifetime of these conduction electrons is longer than the laser pulse length, the material will behave as a metal during the remaining interaction with the laser pulse [3]. A typical carrier lifetimes

of sapphire are in the range of 20 – 200 ps [37] and these durations are definitely longer than a pulse duration (τ = 300 fs) therefore such a surface can support surface plasmons (SPs). Consequently we consider, that the nanogratings form due to initial direct surface plasmons-laser interference and the subsequent grating-assisted SP-laser coupling [36].

To highlight the advantages of deep UV (λ = 206 nm) laser pulses in the ablation of sapphire we did the same experiment with the first harmonic (λ = 1030 nm) under similar conditions (detailed system description is provided in 2.1 section). SEM images of grooves, formed on sapphire's surface are depicted in Fig. 11.

The same PO values were used during infrared laser ablation as in the deep UV experiment. However, fluence values had to be several times higher for the ablation to occur because for the excitation of the electrons across the bandgap of sapphire more photons are required when longer wavelengths are used. The absorption process is more probable when a fewer number of photons is required and the defect saturation region is achieved with fewer pulses in the deep UV case. It can clearly be seen that the decline of ablation quality is evident while using IR pulses instead of deep UV. In addition, the surrounding area is damaged over a wide region even comparable to the groove's width. Thin stripes of a modified material can be seen in the surrounding area, which we presume is attributed to the crystal polishing quality. While the width values of the grooves, ablated using IR pulses are comparable with the ones, ablated using deep UV pulses, depth values were much higher (in the range of 3–6 μm) meaning that the aspect ratio increased. This aspect ratio was excessively large for the topography characterization using optical profilometer. For this purpose the replica of a sample was made using a SYLGARD 184 Silicone Elastomer Base and Sylgard Silicone Elastomer Curing agent mixture with a 10:1 ratio. The resulting surface roughness Sa values are represented in Fig. 11 and are several times higher if compared to the values, obtained using deep UV laser pulses.

4. Conclusions

Our research focused on studying the laser ablation of crystalline c-cut sapphire using femtosecond Deep UV laser pulses to minimize thermal effects on the processing outcomes. We examined how laser processing parameters impact the shape of the ablated micro channels and developed a streamlined process for precise and swift automated characterization of ablation outcomes, which is also valid while using different experimental setups or different conditions. This approach aids in quickly understanding the results and effects of laser ablation. Two distinct ablation regimes were identified: an *inefficient* regime (PO < 97.6%) resulting in shallow, rough structures, and an *efficient* regime (PO > 97.6%) producing deep structures with low roughness (less than 100 nm). Within the efficient regime, by adjusting the laser pulse energy between 1.1 – 1.6 μJ, it is possible to control the full-width at half-maximum (FWHM) values of channels within the range of 7–10 μm and their depth within the range of 3.5–4 μm. These optimized laser parameters ensure both high-quality and high-throughput results. The use of femtosecond deep UV laser pulses with high photon energy and short pulse duration ensures that the removal of sapphire material is not driven by thermal processes. The absence of melted and resolidified areas, as seen in SEM images, suggests that melting and solidification are not involved. The grain-like structure of the ablated regions implies a photomechanical mechanism for material breakup and ejection. When starting from relatively low laser fluence levels, material removal has a nondeterministic nature of damage suggesting that the ablation might originate from impurities with higher absorption rates that are distributed randomly. Additionally, near-subwavelength ripples with a period in the interval of Λ = (155 – 200) nm are observed in regions of low fluence, oriented perpendicular to the laser beam's polarization. We attribute their formation mechanism to direct surface plasmon-laser interference. At higher fluence levels, the ablation process intensifies due to the incubation effect. The same experiment under similar conditions was repeated using longer wavelength (1030 nm) and the decline of the ablation quality is evident. Modified region average surface roughness Sa values of the channels, ablated using IR are several times higher if compared to the values obtained using deep UV pulses.

Funding

This research has been carried out in the framework of the "Universities' Excellence Initiative" program by the Ministry of Education, Science and Sports of the Republic of Lithuania under the agreement with the Research Council of Lithuania (project No. S-A-UEI-23-6).

CRediT authorship contribution statement

Dominyka Stonyte: Writing – review & editing, Writing – original draft, Visualization, Software, Methodology, Investigation, Formal analysis, Data curation, Conceptualization. **Vytautas Jukna:** Writing – review & editing, Supervision, Conceptualization. **Darius Gailevicius:** Writing – review & editing. **Domas Paipulas:** Writing – review & editing, Supervision, Resources, Funding acquisition.

Declaration of competing interest

The authors declare that they have no known competing financial interests or personal relationships that could have appeared to influence the work reported in this paper.

Data availability

Data will be made available on request.

Acknowledgments

Conceptualization was carried out by D.S., D.P, and V.J. The experiments were carried out by D.S. under the supervision of D.P., and V.J. Data post-processing program was developed by D.S. under the supervision of V.J. The data analysis and writing of the draft were carried out by D.S. The revision of the draft and editing was carried out by V.J., D.G., and D.P. All authors have read and agreed to the published version of the manuscript.

References

[1] X.C. Wang, G.C. Lim, H.Y. Zheng, F.L. Ng, W. Liu, S.J. Chua, Femtosecond pulse laser ablation of sapphire in ambient air, Appl. Surf. Sci. 228 (1) (2004) 221–226, http://dx.doi.org/10.1016/j.apsusc.2004.01.009.

[2] D. Ashkenasi, A. Rosenfeld, H. Varel, M. Wähmer, E. E.B. Campbell, Laser processing of sapphire with picosecond and sub-picosecond pulses, Appl. Surf. Sci. 120 (1–2) (1997) 65–80, http://dx.doi.org/10.1016/S0169-4332(97)00218-3.

[3] H. Varel, M. Wähmer, A. Rosenfeld, D. Ashkenasi, E.E.B. Campbell, Femtosecond laser ablation of sapphire: Time-of-flight analysis of ablation plume, Appl. Surf. Sci. 127–129 (1998) 128–133, http://dx.doi.org/10.1016/S0169-4332(97)00622-3.

[4] S. Kawaminami, K. Mochizuki, N. Adachi, T. Ota, Crystal growth of large sapphire and its optical properties, J. Ceram. Soc. Jpn. 122 (1428) (2014) 695–700, http://dx.doi.org/10.2109/jcersj2.122.695.

[5] Siyu Liu, Zhipeng Qu, Mingyun Lv, Guangyuan Ma, Damage and failure mechanism of bullets impact sapphire based on LS-DYNA, in: Proceedings of the 4th Annual International Conference on Material Engineering and Application, ICMEA 2017, Atlantis Press, 2018/02, pp. 178–182, http://dx.doi.org/10.2991/icmea-17.2018.41.

[6] J. Romijn, S. Vollebregt, V.G. de Bie, L.M. Middelburg, B. El Mansouri, H.W. van Zeijl, A. May, T. Erlbacher, J. Leijtens, G. Zhang, P.M. Sarro, Microfabricated albedo insensitive sun position sensor system in silicon carbide with integrated 3D optics and CMOS electronics, Sensors Actuators A 354 (February) (2023) 114268, http://dx.doi.org/10.1016/j.sna.2023.114268.

[7] W. Tian, Y. Wu, T. Wu, L. Dou, X. Cao, J. Li, Mechanisms and performance analysis of gan-based micro-LED grown on pattern sapphire substrate by laser lift-off process, ECS J. Solid State Sci. Technol. 11 (4) (2022) 46001, http://dx.doi.org/10.1149/2162-8777/ac63e5.

[8] R. Lee, E. Tucker, A.A. Neuber, A. Hewitt, R. Clark, H. Hudyncia, T. Buntin, D. Barnett, J.C. Dickens, J.J. Mankowski, W.A. Harrison, High-speed imaging of polymer-bonded explosives under mechanical stresses, in: IEEE International Pulsed Power Conference, Vol. 2019-June, IEEE, 2019, pp. 1–4, http://dx.doi.org/10.1109/PPPS34859.2019.9009758.

[9] N.R. Gottumukkala, M.C. Gupta, Laser processing of sapphire and fabrication of diffractive optical elements, Appl. Opt. 61 (9) (2022) 2391, http://dx.doi.org/10.1364/AO.452810.

[10] Bin L., Qiusheng Y., Jisheng P., Jiabin L., Zhanliang H., Influences of processing parameters on metal-bonded diamond wheel wear when grinding a sapphire wafer, Diam. Relat. Mater. 113 (January) (2021) 108275, http://dx.doi.org/10.1016/j.diamond.2021.108275.

[11] Youkang Y., Yufei G., Chunfeng Y., Sawing characteristics of diamond wire cutting sapphire crystal based on tool life cycle, Ceram. Int. 47 (19) (2021) 26627–26634, http://dx.doi.org/10.1016/j.ceramint.2021.06.070.

[12] David M. Allen, Roxana Redondo, Maximilien Dany, Fabrication methods for the manufacture of sapphire microparts, Microsyst. Technol. 18 (11) (2012) 1835–1841, http://dx.doi.org/10.1007/s00542-012-1484-2.

[13] G. Nanz, L.E. Camilletti, Modeling of chemical-mechanical polishing: a review, 8 (4) (1995) 382–389.

[14] Qiuling W., Pengcheng Z., Guanghua C., Feng J., Xizhao L., Crystalline orientation effects on material removal of sapphire by femtosecond laser irradiation, Ceram. Int. 45 (17) (2019) 23501–23508, http://dx.doi.org/10.1016/j.ceramint.2019.08.056.

[15] S.K. Sundaram, E. Mazur, Inducing and probing non-thermal transitions in semiconductors using femtosecond laser pulses, Nat. Mater. 1 (4) (2002) 217–224, http://dx.doi.org/10.1038/nmat767.

[16] Yang L., Huagang L., Minghui H., High-quality sapphire microprocessing by dual-beam laser induced plasma assisted ablation, Opt. Express 28 (5) (2020) 6242, http://dx.doi.org/10.1364/OE.381268.

[17] X. Fang, S. Wang, B. Li, Theoretical and experimental studies on ultraviolet nanosecond laser micromachining of sapphire, Integr. Ferroelectr. 230 (1) (2022) 179–191, http://dx.doi.org/10.1080/10584587.2022.2102811.

[18] T.C. Chen, R.B. Darling, Parametric studies on pulsed near ultraviolet frequency tripled Nd: YAG laser micromachining of sapphire and silicon, J. Mater. Process. Technol. 169 (2) (2005) 214–218, http://dx.doi.org/10.1016/j.jmatprotec.2005.03.023.

[19] Quanli Zhang, Qiwen Wang, Zhen Zhang, Yucan Fu, Jiuhua Xu, Surface microtexture on sapphire fabricated by laser ablation trajectory regulation, Chin. J. Aeronaut. 35 (3) (2022) 525–536, http://dx.doi.org/10.1016/j.cja.2021.10.009.

[20] C.S.M. Lye, Z.K. Wang, Y.C. Lam, Mechanism and effects of surface morphology on absorption characteristics in ultrashort pulse laser processing of sapphire, Appl. Surf. Sci. 542 (September 2020) (2021) 148734, http://dx.doi.org/10.1016/j.apsusc.2020.148734.

[21] A. Crunteanu, P. Hoffmann, M. Pollnau, Ch Buchal, Comparative study on methods to structure sapphire, Appl. Surf. Sci. 208–209 (1) (2003) 322–326, http://dx.doi.org/10.1016/S0169-4332(02)01382-X.

[22] X. Wei, X.Z. Xie, W. Hu, J.F. Huang, Polishing sapphire substrates by 355nm ultraviolet laser, Int. J. Opt. 2012 (2012) http://dx.doi.org/10.1155/2012/238367.

[23] H. Horisawa, H. Emura, N. Yasunaga, Surface machining characteristics of sapphire with fifth harmonic yag laser pulses, Vacuum 73 (3–4) (2004) 661–666, http://dx.doi.org/10.1016/j.vacuum.2003.12.065.

[24] Q. Wang, Q. Zhang, Z. Zhang, W. Wang, J. Xu, Material removal and surface formation mechanism of C-plane sapphire in multipass ablation by a nanosecond UV laser, Ceram. Int. 46 (13) (2020) 21461–21470, http://dx.doi.org/10.1016/j.ceramint.2020.05.244.

[25] A. Butkute, R. Sirutkaitis, D. Gailevicius, D. Paipulas, V. Sirutkaitis, Sapphire selective laser etching dependence on radiation wavelength and etchant, Micromachines 14 (1) (2023) http://dx.doi.org/10.3390/mi14010007.

[26] D. Smith, Soon Hock Ng, A. Tang, T. Katkus, D. Moraru, S. Juodkazis, Crystalline flat surface recovered by high-temperature annealing after laser ablation, Photonics 10 (5) (2023) http://dx.doi.org/10.3390/photonics10050594.

[27] J.M. Liu, Simple technique for measurements of pulsed Gaussian-beam spot sizes, Opt. Lett. 7 (5) (1982) 196, http://dx.doi.org/10.1364/ol.7.000196.

[28] ISO 25178-3, Geometrical Product Specifications (GPS) - Surface Texture: Areal - Part 3: Specification Operators (ISO 25178-3:2012), Standard, 2012.

[29] American Society of Mechanical Engineers, American Society of Mechanical Engineers Standards Committee B46, Classification and designation of surface qualities, surface texture: surface roughness, waviness, and lay, 2020.

[30] ISO 25178-2, Geometrical Product Specifications (GPS) - Surface Texture: Areal - Part 2: Terms, Definitions and Surface Texture Parameters (ISO 25178-2:2021), Standard, 2022.

[31] M. Wang, W. Mei, Y. Wang, Simulation of femtosecond laser ablation sapphire based on free electron density, Opt. Laser Technol. 113 (December 2018) (2019) 123–128, http://dx.doi.org/10.1016/j.optlastec.2018.12.007.

[32] M.E. Shaheen, J.E. Gagnon, B.J. Fryer, Studies on laser ablation of silicon using near IR picosecond and deep UV nanosecond lasers, Opt. Lasers Eng. 119 (2019) 18–25, http://dx.doi.org/10.1016/j.optlaseng.2019.02.003.

[33] J. Ma, M.B. Airola, M.E. Thomas, J.B. Spicer, Weak absorption and scattering losses from the visible to the near-infrared in single-crystal sapphire materials, Opt. Eng. 59 (08) (2020) 1, http://dx.doi.org/10.1364/FIO.2019.JW3A.36.

[34] B. Momgaudis, M. Vengris, A. Melninkaitis, Time-resolved holographic study of laser-induced fatigue in bulk of sapphire and fused silica, Opt. Contin. 1 (4) (2022) 759, http://dx.doi.org/10.1364/OPTCON.453503.

[35] R. Vilar, S.P. Sharma, A. Almeida, L.T. Cangueiro, V. Oliveira, Surface morphology and phase transformations of femtosecond laser-processed sapphire, Appl. Surf. Sci. 288 (2014) 313–323, http://dx.doi.org/10.1016/j.apsusc.2013.10.026.

[36] M. Huang, F. Zhao, Y. Cheng, N. Xu, Z. Xu, Origin of laser-induced near-subwavelength ripples: interference between surface plasmons and incident laser, ACS Nano 3 (12) (2009) 4062–4070, http://dx.doi.org/10.1021/nn900654v.

[37] F. Wang, J. Shan, E. Knoesel, M. Bonn, T.F. Heinz, Electronic charge transport in sapphire studied by optical-pump/THz-probe spectroscopy, in: Kong-Thon Tsen, Jin-Joo Song, Hongxing Jiang (Eds.), Ultrafast Phenomena in Semiconductors and Nanostructure Materials VIII, Vol. 5352, SPIE, 2004, pp. 216–221, http://dx.doi.org/10.1117/12.532505.